

**Macroscopic plastic deformation through an integrated first-principles calculations and  
finite element simulations: Application to nickel single crystal**

Shipin Qin<sup>1</sup>, Shun-Li Shang<sup>1</sup>, John Shimanek<sup>1</sup>, Zi-Kui Liu<sup>1</sup>, and Allison M. Beese<sup>1,2,\*</sup>

<sup>1</sup> *Department of Materials Science and Engineering, The Pennsylvania State University,  
University Park, PA 16802, USA*

<sup>2</sup> *Department of Mechanical Engineering, The Pennsylvania State University, University Park,  
PA 16802, USA*

*\* Corresponding author: amb961@psu.edu*

**Abstract:**

The crystal plasticity finite element method (CPFEM) has been widely adopted to describe mechanical properties of single crystals. Even though CPFEM explicitly considers the deformation mechanisms of single crystals, the parameters used within the CPFEM framework are typically determined through fitting of macroscopic experimental results. In the present work, a multiscale approach that combines first-principles calculations of individual phases and CPFEM is proposed to predict the strain hardening behavior of pure Ni single crystal. Density functional theory (DFT)-based first-principles calculations were used to predict the strain hardening behavior on the slip systems of Ni single crystal in terms of the Peierls stress calculated from ideal shear strength and elastic properties. The DFT-based predictions based on pure edge and pure screw dislocations provided parameter inputs for a CPFEM framework. Actual plastic deformation of pure Ni is more complex, initially involving edge dislocations, and eventually also the interactions of edge dislocations that result in jogs with screw dislocation character. Hence, a model that

combines influences of both edge and screw dislocations was proposed. It was found that CPFEM predictions based solely on edge dislocations agreed well with experiments at small strains ( $< 0.06$  in the present work), while the predictions adopting the proposed edge-screw model fully capture experimental data at large deformations.

**Keywords:** Crystal plasticity; Single crystal deformation; Multi-scale modeling; First-principles calculations; Peierls stress

## 1. Introduction

Due to their high ductility, the mechanical properties of face-centered cubic (fcc) single crystals have been widely investigated, providing insight into the mechanisms of their plasticity at different deformation stages. The mechanical response of single crystals is typically described in the literature by the resolved shear stress-strain behavior on particular slip systems within the single crystal [1]. Pure Ni single crystal is one such example, whose mechanical properties have been investigated through both experiments [2–4] and simulations [5,6].

Prior experimental work on Ni single crystal has focused on determining the resolved shear stress-strain behavior on its slip systems. For example, Haasen [2] performed tension tests on Ni single crystal wire along different orientations, and at different temperatures, and revealed an orientation-independent inverse relationship between the initial critical resolved shear stress (CRSS, represented by  $\tau_0$  in the present work) and temperature. Yao et al. [7] performed dogbone tension tests on non-irradiated and irradiated single crystal specimens of pure Ni and found that yield stress rose with increasing irradiation dose.

The crystal plasticity finite element method (CPFEM) was developed based on the understanding of plastic deformation of crystals through slip mechanisms, and has been viewed as a promising approach for modeling the mechanical behavior of single crystals [8]. Within the framework of CPFEM, the kinematics of slip can be described through a dyadic form of the velocity gradient, which can be decomposed into a symmetric part (deformation) and an antisymmetric part (rotation) [8]. While the kinematic description is similar for most CPFEM models, individual models differ in their constitutive framework and can be generally categorized into either phenomenological models or physics-based models [8], with the key difference being whether or not the models explicitly consider the evolution of dislocation density. In physics-

based models, the flow stress is calculated based on the evolution of dislocation density, with explicit consideration of dislocation formation, annihilation, and interactions. Conversely, in phenomenological models, the evolution of dislocation density is either modeled without accounting for underlying physical mechanisms or not explicitly considered, and the CRSS for each slip system is taken as a microstructural state variable, whose evolution is described by a hardening law that is generally a function of the shear strain on each slip system.

Both phenomenological [9–14] and physics-based models [15–19] have been shown to be able to capture experimentally observed mechanical behavior of single crystals and polycrystals. However, most work in the literature relies on macroscopic stress-strain curves to calibrate model parameters, even for physics-based models [6,9,10,20,21]. One example is the physics-based model proposed by Ma and Roters [20], whose calibration used macroscopic stress-strain curves partially because some parameters like the initial dislocation density and the activation energy for dislocation slip and dislocation climb are very challenging to determine experimentally or computationally. Nevertheless, there are efforts in the literature to determine the parameters through lower length-scale computations [22,23]. For example, when modeling the mechanical behavior of three Ti-Nb alloys, Ma et al. [22] determined the elastic constants in their CPFEM model through density functional theory (DFT)-based first-principles calculations, while the plasticity behavior in their model was calibrated with a macroscopic mechanical test.

Due to the complexity of the mechanisms associated with strain hardening, some researchers have concluded that an ab initio theory of strain hardening is unlikely [24,25]. However, efforts have been made to model strain hardening behavior based on the underlying physics [26–30]. One approach, taken by Langer et al. [26], involved the application of thermodynamic principles to predict the strain hardening behavior of Cu under different temperatures and strain rates. The

authors adopted the concept of an effective temperature that characterizes the internal state of disorder and related it to steady-state properties like the quasi-equilibrium density of dislocations and the plastic strain rate. In another approach, Vattré [28] coupled 3D dislocation dynamics (DD) simulations with a finite element method to perform crystal plasticity simulations. The authors considered the dislocation network evolution and the short-range dislocation-dislocation interactions through DD simulations, and considered long-range dislocation-dislocation interactions through finite element simulations with a non-local constitutive law. In addition, some parameters in CPFEM models are directly related to values that can be computed with DFT-based calculations, including the CRSS of a slip system (the Peierls stress) as explored in the present study [31,32].

The present work aims to develop an approach to determine key parameters in a phenomenological CPFEM model through DFT-based calculations at the atomic and electronic length scales. By applying pre-strains in these calculations, the interaction between slip systems was simulated, and the resolved shear stress-strain relationships for pure edge and pure screw dislocations were predicted using the Peierls-Nabarro model. The CPFEM model parameters were determined from DFT-based predictions and were then adopted for predicting the macroscopic stress-strain curves of various single crystal tensile tests. Since the dislocation population in an fcc crystal is edge dominant only under stage I deformation [33–37], CPFEM simulations for pure edge dislocations were first performed to predict the strain hardening behavior at small strains. At large strains, in which the dislocation population within an fcc crystal is a mixture of edge and screw types [33–37], a simple model is proposed to combine the DFT-based predictions of the two dislocation types. CPFEM simulations that consider both types of dislocations were performed to predict the strain hardening behavior at large strains.

## 2. Methodology

### 2.1 Crystal plasticity model

Based on the kinematics of deformation, the deformation gradient  $\mathbf{F}$  can be multiplicatively decomposed as,  $\mathbf{F} = \mathbf{F}_e \mathbf{F}_p$ , where  $\mathbf{F}_e$  is the elastic deformation gradient and  $\mathbf{F}_p$  the plastic deformation gradient [8,38]. The stress in a crystal can be calculated by  $\boldsymbol{\sigma} = \mathbb{C} : \boldsymbol{\varepsilon}_e$ , where  $\boldsymbol{\sigma}$  is the Cauchy stress tensor,  $\mathbb{C}$  the fourth-order elastic stiffness tensor, and  $\boldsymbol{\varepsilon}_e$  the work-conjugate elastic strain related to  $\mathbf{F}_e$  via  $\boldsymbol{\varepsilon}_e = \frac{1}{2}(\mathbf{F}_e^T \mathbf{F}_e - \mathbf{I})$ , where  $\mathbf{I}$  is the second order identity tensor [39,40]. Since  $\mathbb{C}$  is symmetric, it can be written as a 2D matrix,  $c_{ij}$ , following the Mandel notation. For fcc metals there are only three non-zero and independent elastic constants:  $c_{11}$ ,  $c_{12}$ , and  $c_{44}$ .

In the framework of crystal plasticity, the relationship between the macroscopic plastic deformation gradient and the slip on a single crystallographic slip system,  $\alpha$ , is given as [41]:

$$\mathbf{L}_p = \sum_{\alpha=1}^l \dot{\gamma}^\alpha \mathbf{m}^\alpha \otimes \mathbf{n}^\alpha \quad \text{Eq. 1}$$

where

$$\mathbf{L}_p = \dot{\mathbf{F}}_p \mathbf{F}_p^{-1} \quad \text{Eq. 2}$$

is the macroscopic plastic velocity gradient,  $\dot{\gamma}^\alpha$  is the shear strain rate on slip system  $\alpha$ ,  $l$  is the total number of slip systems (12 for fcc crystals), and  $\mathbf{m}^\alpha$  and  $\mathbf{n}^\alpha$  are the slip direction and slip plane normal in the configuration before deformation, respectively. The shear strain rate on slip system  $\alpha$ ,  $\dot{\gamma}^\alpha$ , under an applied resolved shear stress on that slip system,  $\tau^\alpha$ , is calculated as [41]:

$$\dot{\gamma}^\alpha = \dot{\gamma}_0 \left| \frac{\tau^\alpha}{\tau_c} \right|^n \text{sgn}(\tau^\alpha) \quad \text{Eq. 3}$$

where  $\dot{\gamma}_0$  is a reference shear rate,  $\tau_c^\alpha$  is the CRSS characterizing the current strength of slip system  $\alpha$ , and  $n$  is an exponent describing strain rate sensitivity. In the literature,  $\dot{\gamma}_0 = 0.001 \text{ s}^{-1}$  and  $n = 20 \sim 100$  [5,9,10,39,42,43] are typically adopted for rate-independent material behavior.  $\tau_c^\alpha$  is similar to flow stress at the macroscopic scale and evolves with strain. Its evolution due to the shear strain on any slip system  $\beta$  is given by:

$$\dot{\tau}_c^\alpha = \sum_{\beta=1}^l h_{\alpha\beta} |\dot{\gamma}^\beta| \quad \text{Eq. 4}$$

where  $h_{\alpha\beta}$  is the hardening matrix. Note that since all 12 slip systems in fcc crystals are equivalent, slip system  $\alpha$  and slip system  $\beta$  in the above equations are arbitrary. Eq. 4 describes how the CRSS, initially  $\tau_0$ , changes with shear strain on individual slip systems. Thus, it provides a slip system level strain hardening relationship, with the shape of this curve being determined by the form of  $h_{\alpha\beta}$ . Many forms of  $h_{\alpha\beta}$  have been proposed, while a form presented by Peirce et al. [44] is adopted in the present work for its minimal number of parameters, the simplicity of its mathematical form, and the physical interpretability of the individual parameters. Specifically, Peirce et al. [44] proposed that:

$$h_{\alpha\beta} = q_{\alpha\beta} \left[ h_0 \operatorname{sech}^2 \left| \frac{h_0 \gamma}{\tau_s - \tau_0} \right| \right] \quad \text{Eq. 5}$$

where

$$q_{\alpha\beta} = \begin{cases} 1, & \alpha = \beta \\ 1.4, & \alpha \neq \beta \end{cases} \quad \text{Eq. 6}$$

characterizes the difference between self-hardening ( $\alpha = \beta$ ) and latent hardening ( $\alpha \neq \beta$ ). With this form, the slip system level strain hardening curve increases monotonically with a decreasing

slop and approaches a saturation value asymptotically. The initial slop of this curve is controlled by  $h_0$ , and the saturation value is controlled by  $\tau_s$ .

With the above model, prediction of the strain hardening behavior of fcc single crystals is simplified to the following three parts:

- Prediction of the initial CRSS ( $\tau_0$ );
- Prediction of the initial strain hardening behavior at small strains ( $h_0$ );
- Prediction of the strain hardening saturation behavior at large strains ( $\tau_s$ ).

The present study predicted the first two parts through DFT-based computations, while  $\tau_s$  was not predicted in this study, but was taken from results reported in the literature.

## 2.2 First-principles calculations of Peierls stress

In the model described above, the initial CRSS,  $\tau_0$ , is the minimum shear stress required to initiate plastic deformation [45]. For perfect crystal lattices without any defects, this corresponds to the ideal shear strength  $\tau_{IS}$ , while for crystal lattices with pre-existing dislocations, this corresponds to the Peierls stress  $\tau_P$ . The current study aims to predict the strain hardening behavior at room temperature in single crystals in which dislocations are present, therefore,  $\tau_0$  corresponds to the Peierls stress  $\tau_P$ , which is predicted using first-principles calculations. The initial strain hardening behavior, or  $h_0$ , can be taken from the  $\tau_P$  values as a function of strain. In the current study, the evolution of Peierls stress is calculated by applying increasing values of pre-strain to the lattice in the DFT-based calculations.

It should be noted that all DFT-based calculations of CRSS in the present work were performed at 0 K for simplification, while all experimental data were taken at room temperature. This

simplification is appropriate because, for pure metals, the CRSS values at 0 K are close to those at room temperature [46]. Additionally, previous calculations have indicated that properties from DFT-based calculations at 0 K are comparable to experimental data measured at room temperature (298 K) for many properties. For example, the predicted difference of enthalpy of formation is negligible between 0 K and room temperature ( $< 0.2$  kJ/mol for metal sulfides [47]), the predicted bulk moduli of Ni and Ni<sub>3</sub>Al decrease about 9 GPa (5 %) from 0 K to room temperature [48], and the predicted ideal shear strength of Ni decreases about 0.1 GPa (2 %) [49].

### 2.2.1. Peierls stress, $\tau_p$ , from ideal shear strength, $\tau_{IS}$ , and elastic properties

In the present work, the Peierls stress,  $\tau_p$ , is estimated using the Peierls-Nabarro model [31,32] as shown in Eq. 7 for a wide dislocation [50].

$$\tau_p = \frac{Kb}{a} \exp(-2\pi\zeta/d) \quad \text{Eq. 7}$$

Here,  $b$  is the Burgers vector,  $a$  is the row spacing of atoms within the slip plane (for example,  $a = a_0\sqrt{6}/4$ , where  $a_0$  is the lattice parameter, for the case of  $\{111\}\langle 11\bar{2} \rangle$  shear deformation of an fcc lattice), and  $\zeta$  is the half-width of the dislocation, given as:

$$\zeta = \frac{Kb}{4\pi\tau_{IS}} \quad \text{Eq. 8}$$

where  $\tau_{IS}$  is the ideal strength. The elastic factor,  $K$ , can be expressed as follows for an isotropic (iso) crystal [50],

$$K_{iso} = \mu \left( \frac{\sin^2\theta}{1-\nu} + \cos^2\theta \right) \quad \text{Eq. 9}$$

where  $\mu$  is shear modulus,  $\nu$  is Poisson's ratio, and  $\theta$  is the angle between the dislocation line and its Burgers vector ( $0^\circ$  for screw dislocations and  $90^\circ$  for edge dislocations). The  $K$  values are

direction-dependent for an anisotropic crystal. For example, for an edge dislocation aligned with the z-direction, with a Burgers vector  $\mathbf{b} = (b_x, b_y, 0)$ , the corresponding  $K_{e_x}$  of edge dislocation along the x-direction is given by [51],

$$K_{e_x} = (\bar{c}'_{11} + c'_{12}) \left[ \frac{c'_{66} (\bar{c}'_{11} - c'_{12})}{(\bar{c}'_{11} + c'_{12} + 2c'_{66}) c'_{22}} \right]^{1/2} \quad \text{Eq. 10}$$

where  $\bar{c}'_{11} = (c'_{11} c'_{22})^{1/2}$  and  $c'_{ij}$  indicates the transformed elastic constants onto the slip system of interest. In the present work, the transformed lattice vectors of fcc Ni are parallel to the  $[11\bar{2}]$ ,  $[\bar{1}10]$ , and  $[111]$  directions of the conventional fcc lattice, i.e., the  $\mathbf{a}_{\text{orth}}$  (x),  $\mathbf{b}_{\text{orth}}$  (y), and  $\mathbf{c}_{\text{orth}}$  (z) directions, respectively; see Figure 1a. Notably  $K_{e_x} = K_{e_y} (= K_e)$  for edge dislocations along the x- and y-directions for the present fcc Ni represented by the orthorhombic cell as shown in Figure 1a. The elastic factor for screw dislocations,  $K_s$ , of an anisotropic crystal is given by [51],

$$K_s = (c'_{44} c'_{55} - c'^2_{45})^{1/2} \quad \text{Eq. 11}$$

The ideal shear strength in Eq. 8 can be predicted directly by pure alias shear – a deformation similar to the dislocation motion that constitutes slip [49,52,53]. Alias shear involves only one sliding layer ( $n = 1$ ) with the atoms in other layers initially remaining in their original positions [49,52,53]; see Figure 1b. The relaxations of a pure alias shear include all degrees of freedom of a supercell except for the fixed shear angle as well as other constraints such as the pre-strain deformation discussed below.

Considering the major slip system in fcc lattices of  $\{111\}\langle 110 \rangle$  as well as the splitting of the  $1/2[\bar{1}10]$  dislocation into two Shockley partials on the (111) plane via  $1/2[\bar{1}10] \rightarrow 1/6[\bar{2}11] + 1/6[\bar{1}2\bar{1}]$  [49,51,53], a 6-atom orthorhombic supercell was adopted for fcc Ni with its lattice

vectors  $\mathbf{a}_{\text{orth}}$ ,  $\mathbf{b}_{\text{orth}}$ , and  $\mathbf{c}_{\text{orth}}$  of the respective lengths  $0.5\sqrt{6}a_0$ ,  $0.5\sqrt{2}a_0$ , and  $\sqrt{3}a_0$  ( $a_0$  is the lattice parameter of fcc Ni) parallel to the  $[11\bar{2}]$ ,  $[\bar{1}10]$ , and  $[111]$  directions, respectively; see Figure 1a. After  $\{111\}\langle 11\bar{2}\rangle$  alias shear, the deformed lattice vector matrix  $\mathbf{R}'$  is given as:

$$\mathbf{R}' = \mathbf{R}\mathbf{D} \quad \text{Eq. 12}$$

where  $\mathbf{R}$  is the undeformed lattice vector matrix and  $\mathbf{D}$  is the deformation matrix, given as:

$$\mathbf{D} = \begin{bmatrix} 1 & 0 & 0 \\ 0 & 1 & 0 \\ \gamma_{112} & \gamma_{110} & 1 \end{bmatrix} \quad \text{Eq. 13}$$

where  $\gamma$  is the magnitude of the engineering shear strain, i.e., the ratio of shear displacement to the height of the supercell [49,52],  $\gamma_{112}$  is the shear strain along the  $[11\bar{2}]$  direction, and  $\gamma_{110}$  is the pre-strain along the  $[\bar{1}10]$  direction. Note that the pre-strain along  $[\bar{1}10]$  creates a strain field on the close packed plane analogous to that created by slipping, while the shear strain long  $[11\bar{2}]$  allows DFT-based calculations to probe the maximum ideal shear strength on the partial slip system. Thus, the above operations can be interpreted as probing the dependence of  $\tau_{\text{IS}}$  on one slip system due to the shear strain of another slip system ( $[\bar{1}10]$ ), or equivalently, the strain hardening behavior on a slip system.

Elastic properties in Eq. 9 through Eq. 11 can be predicted by computing stresses under given strains by means of first-principles calculations and Hooke's law, as previously shown [54,55]. The imposed strains used here to predict the single crystal elastic constants,  $c_{ij}$ , are  $\pm 0.007$  and  $\pm 0.013$ . Starting from single crystal  $c_{ij}$  values, average elastic properties, such as the shear modulus and Poisson's ratio, were calculated using the Voigt isostrain approach, which is more representative of the local strain fields around dislocations than the Reuss isostress average

[51,56]. Using these elastic constants, Peierls stresses were predicted for single crystals, assuming both isotropic (Eq. 9) and anisotropic (Eq. 10 and Eq. 11) elastic behavior.

### 2.2.2. Details of first-principles calculations

All DFT-based first-principles calculations in the present work were performed by the Vienna *Ab initio* Simulation Package (VASP) [57]. The ion-electron interaction was described by the projector augmented wave (PAW) method [58]; the exchange-correction functional was depicted by the generalized gradient approximation (GGA, PW91) as parameterized by Perdew et al. [59]; and the core configuration of [Ar] was employed for Ni as recommended by VASP. In VASP calculations, the  $k$ -point meshes of  $10 \times 16 \times 7$  were used for the 6-atom orthorhombic supercell (see Figure 1a); the cutoff energy of 337 eV (i.e., the precision of “high” used in VASP) was employed for the plane-wave basis set; and the energy convergence criterion of electronic self-consistency was selected as  $10^{-5}$  eV per supercell for all calculations. The reciprocal-space energy integration was performed by the Methfessel-Paxton [60] technique with a 0.2 eV smearing width, which can result in accurate total energies as well as stresses. Concerning pure alias shear deformation, an external optimizer GADGET developed by Bučko et al. [61] was used to control both stresses and forces acting on each atom during VASP calculations. The relaxed stresses (except for the shear stresses due to the fixed  $\gamma_{112}$  and/or  $\gamma_{110}$  values) were less than 0.15 GPa, and the forces acting on atoms were less than 0.03 eV/Å. Spin polarization was considered in all first-principles calculations due to the magnetic nature of Ni.

Aiming toward understanding layer-dependent ideal shear strength, ancillary DFT-based calculations of pure alias shear along  $\{111\}\{11\bar{2}\}$  were also performed using the 6-atom (3-layer), 12-atom (6-layer), and 18-atom (9-layer) orthorhombic supercells based on the structure shown in

Figure 1a. The corresponding  $k$ -point meshes were  $10 \times 16 \times 7$ ,  $9 \times 16 \times 3$ , and  $7 \times 12 \times 2$ , respectively. In addition, phonon calculations were also carried out to explore the origin of layer-dependent  $\tau_{IS}$  in terms of the 6-atom (3-layer) and the 12-atom (6-layer) orthorhombic cells after  $\{111\}\langle 11\bar{2}\rangle$  pure alias shear by applying the same amount of shear displacement ( $0.5 \text{ \AA}$ ). These phonon calculations were performed by the supercell approach [62] as implemented in the YPHON code [63,64]. The VASP code was again the computational engine in calculating force constants by the density functional perturbation theory. For both the 3-layer and the 6-layer orthorhombic lattices, the 72-atom supercells together with the  $3 \times 3 \times 2$   $k$ -point meshes were used for phonon calculations. Note that all other conditions used for these ancillary first-principles calculations were the same as the aforementioned settings.

### 3. Results and discussion

#### 3.1 Results from first-principles calculations

##### 3.1.1. Ideal shear strength of fcc Ni with and without pre-strain

Table 1 summarizes the predicted ideal shear strengths of fcc Ni by pure alias shear deformation along  $\{111\}\langle 11\bar{2}\rangle$  without pre-strain, i.e.,  $\gamma_{110} = 0$  (see Eq. 13). It shows that the fewer the number of  $\{111\}$  layers (represented by  $n_{111}$  in the present work), the larger the  $\tau_{IS}$ . The maximum  $\tau_{IS} = 5.15 \text{ GPa}$  for the case of  $n_{111} = 3$ . This  $\tau_{IS}$  value ( $5.15 \text{ GPa}$ ) agrees well with previous predictions around  $5.0 \text{ GPa}$  using pure alias or pure affine shear deformations [49]. The current value also agrees reasonably well with the value estimated from nanoindentation of approximately  $8 \pm 1.5 \text{ GPa}$  [65], with the difference likely due to the measurement being performed on a non-close packed (001) plane [65] and the stabilizing effect of the triaxial stress

state beneath the indenter tip [66]. With increasing  $n_{111}$ , the predicted  $\tau_{IS}$  decreased significantly (for example,  $\tau_{IS} = 2.603$  GPa when  $n_{111} = 9$ ) despite the fact that the absolute displacement distance increased slightly (from 0.780 to 0.798 Å; see Table 1). By considering the limited layers involved in the movement of dislocation cores during experimental slip processes and the experimental estimate of  $\tau_{IS} \sim 8 \pm 1.5$  GPa, the minimum value of  $n_{111} = 3$  and the corresponding  $\tau_{IS} = 5.15$  GPa were selected for further investigation in the present study.

To understand the decrease of  $\tau_{IS}$  with increasing  $n_{111}$ , the stretching force constants are plotted in Figure 2 with phonon calculations for two fcc-based orthorhombic lattices: one with 3 layers (6 atoms) and one with 6 layers (12 atoms) after pure alias shear with the same amount of displacement distance (0.5 Å) applied. Here the force constants, particularly the dominant stretching force constants shown in Figure 2 (as opposed to the significantly smaller bending force constants), provide quantitative understanding of the interaction or bonding between atomic pairs [67,68]. A large and positive force constant indicates strong bonding, while a negative force constant suggests the pair of atoms tend to separate from each other. Figure 2 shows that the maximum stretching force constants from the 3-layer lattice are higher than those from the 6-layer lattice (2.46 versus 2.28 eV/Å<sup>2</sup>), indicating the bonding between atoms becomes weaker with an increasing number of {111} layers during pure alias shear deformation, which results in lower  $\tau_{IS}$  values.

Table 2 shows that the predicted  $\tau_{IS}$  increases and  $\gamma_{112}$  decreases with increasing pre-strain,  $\gamma_{110}$  (see Eq. 13). As discussed in Section 2.1.1, the  $\gamma_{110}$  pre-strain created a strain field on the close packed plane analogous to that created by slipping, thus allowing the DFT-based predictions to be interpreted as the change of Peierls stresses ( $\tau_P$ ) on one slip system due to the shear strain on

another slip system. The  $\tau_{IS}$  values increased from 5.15 to 5.26 GPa as  $\gamma_{110}$  increased from 0 to 0.049, indicating that the existence of pre-strain makes the  $\{111\}\langle 11\bar{2}\rangle$  shear deformation slightly more difficult (Table 2). However, it should be pointed out that this pre-strain does not consider the formation of jogs due to interactions of dislocations of different slip systems, which is the main contributions to strain hardening with increasing dislocation density [51].

### 3.1.2. Elastic properties of fcc Ni with and without pre-strain

Table 3 summarizes the predicted elastic constants of fcc Ni in terms of the 6-atom orthorhombic cell ( $c'_{ij,orth}$ ). Note that by adopting the relationship given by Hirth and Lothe [51],  $c'_{ij,orth}$  can be transformed to  $c_{ij,cub}$ , which are the elastic constants in terms of the 4-atom conventional cubic cell to be compared to experimental data. These predictions (pre-strain  $\gamma_{110} = 0$ ) agree with the experimental elastic constants extrapolated to 0 K [56]. With increasing pre-strain  $\gamma_{110}$  (up to 0.049), Table 3 shows that the  $c'_{ij,orth}$  values remain almost constant under these small  $\gamma_{110}$  values; for example,  $c'_{11,orth} = 338 \sim 341$  GPa.

### 3.1.3. Peierls stress $\tau_P$ of fcc Ni with and without pre-strain

In the present study, the Peierls stress was calculated from Eq. 7. The elastic factor  $K$  in the equation can be calculated by assuming either isotropic (iso) behavior (Eq. 9) or anisotropic (aniso) behavior (Eq. 10 and Eq. 11). In both cases, the value of  $K$  also depends on the dislocation type, i.e., edge (e) vs screw (s). Therefore, there are four versions of the elastic factor (iso-e, iso-s, aniso-e, and aniso-s), resulting in four different Peierls stresses. Further, each version of  $K$  may be calculated by either considering or disregarding the local strain fields imposed at each level of

pre-strain through the adoption of pre-strain dependent or independent elastic constants. In the present study, all calculations of  $K$  accounted for pre-strain. Since the Peierls stress deals only with local deformations as a single dislocation moves the distance of one Burgers vector, elastic properties describing local stress and strain fields are more appropriate than bulk elastic properties calculated without considering any pre-strain. Moreover, by considering pre-strain in the calculation of the elastic factor, each input value of Eq. 7 is calculated using the same initial (pre-strained) simulation conditions.

Table 2 summarizes the predicted Peierls stresses ( $\tau_P$  values) of all four versions at 0 K, compared with experimental  $\tau_0$  values at room temperature [2,3,69,70]. The predicted  $\tau_P$  values of edge dislocations (9.4 to 12.9 MPa with  $\gamma_{110} = 0$ ) agree well with experimental  $\tau_0$  values (5.5 to 19.6 MPa [2,3,7,69–74]), in accordance with the fact that edge dislocations have been shown to be prominent in fcc Ni at small deformations, but those of screw dislocations (117.7 to 308.7 MPa with  $\gamma_{110} = 0$ ) are significantly higher than experiments. According to experimental observations, edge dislocation dipoles are dominant in stage I of fcc single crystal deformation, which can be explained by mutual annihilation of screw segments through cross-slip [33–37]. With increasing  $\gamma_{110}$  pre-strain, the predicted  $\tau_P$  values increase. For example,  $\tau_P$  (iso-e) increased from 12.9 to 16.6 MPa (increase of about 29 %) as  $\gamma_{110}$  increased from 0 to 0.049. The increase of  $\tau_P$  stems mainly from the increase of  $\tau_{IS}$  compared to elastic properties (see Eq. 7 and values in Table 2).

### 3.2 CPFEM model parameters from first-principles calculations

In above, the prediction of Peierls stress was made by assuming pure edge or pure screw dislocations. However, experimental observations in fcc metals have shown that edge dislocations are dominant only under stage I deformation, while under stage II deformation, both types of dislocation are observed [33–37]. Therefore, the pure edge dislocations assumption is only valid under stage I deformation. At large deformations, the predictions based on pure edge and pure screw dislocations must be combined to consider the influence of both types of dislocations. The present study first attempts to predict the mechanical behavior at small deformations when edge dislocations dominate. The combination of edge and screw dislocations and the predictions at large deformations are discussed in Section 3.5.

As discussed in Section 2.2, DFT-based calculations predicted the evolution of CRSS on slip system  $\alpha$  ( $\tau_c^\alpha$ ) due to the shear strain on slip system  $\beta$  ( $\gamma^\beta$ ,  $\alpha \neq \beta$ ,  $\tau_p$  versus  $\gamma_{110}$  in **Table 2**) while all other slip systems remain inactive (i.e., shear strain being zero). In this case, Eq. 4 through Eq. 6 can be simplified as:

$$\dot{\tau}_c^\alpha = 1.4 \left[ h_0 \operatorname{sech}^2 \left| \frac{h_0 \gamma^\beta}{\tau_s - \tau_0} \right| \right] |\dot{\gamma}^\beta|, (\alpha \neq \beta) \quad \text{Eq. 14}$$

where  $h_0$ ,  $\tau_0$ , and  $\tau_s$  are model parameters. By matching the relationship between  $\tau_c^\alpha$  and  $\gamma^\beta$  determined from Eq. 14 (note that  $\tau_c^\alpha = \tau_0$  when  $\gamma^\beta = 0$ ) with that predicted in DFT-based calculations, the values of  $\tau_0$  and  $h_0$  were determined, as shown in Figure 3. Note that DFT-based predictions are limited to only small strains where  $h_0$  and  $\tau_0$  play a dominant role, so a value reported in the literature was adopted for  $\tau_s$  (40 MPa [5]). The determined parameter values are summarized in Table 4. Lastly, the values of the strain rate related parameters in Eq. 3 were assumed ( $\dot{\gamma}_0 = 0.001$  and  $n = 50$ ) following common practice in the literature [5,9,10,39,42,43].

### 3.3 Experimental results in the literature

To show the predictive accuracy of the present approach, models of Ni single crystal tensile tests from the literature incorporated the hardening parameters determined above into the CPFEM framework to evaluate macroscopic stress-strain responses. The experiments considered in the present work include two uniaxial tension tests reported by Haasen [2] on 99.999% purity Ni wire specimens with a diameter of 2.24 mm and a length of 71.12 mm, and a uniaxial tension test reported by Yao et al. [7] on 99.999% purity Ni specimens with a gauge section size of  $2.5 \times 5.5 \times 0.25 \text{ mm}^3$ , both for single crystals. Figure 4a provides the resolved shear stress-strain curves reported in these publications [2,7]. Note that the loading directions with respect to the crystal orientation are different for each test, i.e.,  $\langle \bar{1} 5 10 \rangle$  and  $\langle \bar{1} 2 8 \rangle$  by Haasen [2], and  $\langle 011 \rangle$  by Yao et al. [7].

#### 3.3.1 Interpretation of experimental results

In the aforementioned publications, the authors showed only the resolved shear stress and resolved shear strain data [2,7]. However, it is not straightforward to convert directly measurable quantities in the tests, namely force and displacement, to resolved shear stress and resolved shear strain on slip systems; the conversion process depends on the assumptions made as discussed below [75].

In the work by Yao et al. [7], only one slip system was assumed to be operating. The resolved shear strain  $\gamma$  and the resolved shear stress  $\tau$  under this assumption are calculated as [76–78]:

$$\gamma = \frac{1}{\cos \theta_0} \left[ \sqrt{(1 + \varepsilon^{eng})^2 - \sin^2 \lambda_0} - \cos \lambda_0 \right] \quad \text{Eq. 15}$$

$$\tau = \sigma^{eng} \frac{\cos \theta_0}{1 + \varepsilon^{eng}} \sqrt{(1 + \varepsilon^{eng})^2 - \sin^2 \lambda_0} \quad \text{Eq. 16}$$

where  $\theta_0$  is the initial angle between the loading direction and the slip plane normal direction,  $\lambda_0$  is the initial angle between the loading direction and the slip direction,  $\sigma^{eng}$  is the engineering stress, and  $\varepsilon^{eng}$  is the engineering strain. This approximation assumes that the loading axis continually rotates with respect to the active slip system throughout loading, which is unlikely to be true in finite deformation [1]. Eq. 15 and Eq. 16 were used to calculate the engineering stress-strain curve in the tests in ref. [7].

In the framework of double slip, the rotation of the loading axis with respect to the active slip system is assumed to cease when it reaches a specific orientation. Before reaching this orientation, single slip operates, and the equations above can be applied. After the rotation of the loading axis activates a conjugate slip system, the two slip systems are assumed to operate simultaneously with the same hardening rate, rotating the loading axis along the slip system boundary until reaching a point of stable double glide that prevents further rotation [76]. If  $\mathbf{n}_1$  and  $\mathbf{n}_2$  are the unit normals of the two slip planes, and  $\mathbf{u}_1$  and  $\mathbf{u}_2$  are the unit vectors of the two slip directions, the resolved shear strain  $\gamma$  and resolved shear stress  $\tau$  under the double glide approximation can be calculated as [76,79]:

$$\gamma = \frac{2}{\mathbf{n}_1 \mathbf{u}_2} \ln \left[ 1 + \frac{\mathbf{n}_1 \mathbf{u}_2 \sin \beta_0}{|\mathbf{w}| \cos \theta_0} (\cot \beta - \cot \beta_0) \right] \quad \text{Eq. 17}$$

$$\tau = \sigma^{eng} \frac{|\mathbf{w}|}{2} \cos \beta \left\{ \cos \theta_0 + \frac{\mathbf{n}_1 \mathbf{u}_2}{|\mathbf{w}|} \sin \beta_0 (\cot \beta - \cot \beta_0) \right\} \quad \text{Eq. 18}$$

$$\sin \beta = \frac{\sin \beta_0}{1 + \varepsilon^{eng}} \quad \text{Eq. 19}$$

where  $\mathbf{w} = \mathbf{u}_1 + \mathbf{u}_2$ , and  $\beta_0$  is the angle between the loading direction and  $\mathbf{w}$  at the onset of double glide. Eq. 15 through Eq. 19 were adopted in the present work to calculate the engineering stress-strain curves in Haasen's tests, in which the initial loading direction was  $\langle \bar{1} 5 10 \rangle$  for crystal #6 and  $\langle \bar{1} 2 8 \rangle$  for crystal #18 in ref. [2]. In both tests, the  $\{111\}\langle \bar{1} 0 1 \rangle$  slip system was active first. It was assumed that when the loading direction rotated to  $\langle \bar{5} 5 14 \rangle$  for crystal #6 and to  $\langle \bar{2} 2 9 \rangle$  for crystal #18, double slip began and  $\{\bar{1}\bar{1}1\}\langle 011 \rangle$  started to operate as an additional slip system. The engineering stress-strain curves for all three tests, calculated using the above equations [2,7], are shown in Figure 4b.

### 3.3.2 Evaluation of experimental results

Discrepancies in the reported literature on pure Ni single crystal CRSS and flow behavior stem from differences in material purity, initial dislocation density, and potential experimental uncertainties. A method must therefore be adopted to evaluate these differences so that they may be considered when comparing computational results to experimental data. Here, differences in experimental results were evaluated by comparing their initial CRSS values since the value of the CRSS is independent of the assumptions adopted for converting force-displacement data to resolved shear-stress strain data.

Figure 5 shows the initial CRSS value of pure Ni reported by ten different groups [2,3,7,69–74,80]. Since the value reported by Latanision et al. [80] is significantly higher than the other reported values, it was excluded from evaluation in the present study. The rest of the experimental data all lie between 5 MPa and 20 MPa, and the statistics of these data are shown in Table 5. According to the statistical analysis of the initial CRSS reported by nine different groups over more than 80 years, the experimental data in the literature exhibited a relative error of 43%.

### 3.4 DFT-based CPFEM predictions at small strains

To simulate the tests reported in the literature, the full geometry of the specimens in each test was modeled. All of the specimens were discretized with 0.2 mm hexahedral full integration elements (element type C3D8 [81]) in the gauge region, and the models contain 20,590 elements for the wire specimen by Haasen [2] and 2,176 elements for the dogbone specimen by Yao et al. [7]. In both models, the vertical movement of the bottom nodes was constrained while a uniform vertical displacement was applied to the top nodes. The horizontal movements of all top and bottom nodes of the flat dogbone specimen in Yao et al.'s study were also constrained to avoid potential out-of-plane distortion [78]. The crystal plasticity model was implemented in the commercial finite element software ABAQUS through a user subroutine UMAT [81] originally developed by Huang [41,82].

Figure 6 shows the simulated engineering stress-strain curves compared to the respective experimental results, with Figure 6a, c, and e showing a comparison over a large range and Figure 6b, d, and f focusing on the small strain range. Error bars of 43% were added to the small strain range figures, corresponding to the standard deviation of initial CRSS values reported in the literature and discussed above.

As can be seen from Figure 6, the initial yield stresses in all of the tests were reasonably predicted, and the predictions based on the anisotropic elastic factor  $K_{aniso}$  showed better agreement with experimental data compared to those from  $K_{iso}$ , indicating the anisotropic elastic factor  $K_{aniso}$  within the (111) plane (see Eq. 10, Eq. 11, and Figure 1a) resulted in a better prediction of initial yield stresses of Ni single crystals than if using the isotropic elastic factor,

$K_{iso}$ . Table 6 provides a detailed comparison between experimental and predicted yield stresses for all tests.

At small strains, the strain hardening behavior was reasonably approached by the CPFEM predictions, as the predictions were within the error range up to 10% strain for Haasen's test along the  $\langle \bar{1} 5 10 \rangle$  direction and for Yao et al.'s test, and up to 6% strain for Haasen's test along the  $\langle \bar{1} 2 8 \rangle$  direction. Since the predictions above were made based on the assumption of pure edge dislocations, which is valid only at small deformations, discrepancies at large strains are to be expected (Figure 6).

### 3.5 Modeling and predictions at large strains

As discussed in Section 3.2, the DFT-based predictions based on pure edge and pure screw dislocations need to be combined to accurately predict the strain hardening behavior of fcc metals at large strains. Since experimental observations in the literature [33–37] indicate an increasing influence of screw dislocations with increasing deformation, the following model is proposed in the present study to combine DFT-based results based on edge and screw dislocations:

$$\tau_c^{\alpha,es} = (1 - w\gamma^\beta)\tau_p^{edge} + w\gamma^\beta\tau_p^{screw} \quad \text{Eq. 20}$$

where  $w$  is a weighting factor that controls the contribution from each type of dislocation,  $\gamma^\beta$  is the shear strain on slip system  $\beta$ ,  $\tau_p^{edge}$  and  $\tau_p^{screw}$  are the predicted CRSS in the DFT-based calculations (see Eq. 7) for pure edge and pure screw dislocations, respectively, and  $\tau_c^{\alpha,es}$  is the CRSS on slip system  $\alpha$  (see Eq. 3) considering contributions to the strain hardening from both edge and screw dislocations. Both  $\tau_p^{edge}$  and  $\tau_p^{screw}$  change with  $\gamma^\beta$ . By including  $\gamma^\beta$  in the model, the influence of both types of dislocations are included naturally: (1) edge dislocations are

dominant at small strains ( $\tau_c^{\alpha,es} = \tau_p^{edge}$  when  $\gamma^\beta = 0$ ), and (2) the influence of screw dislocations increases with increasing strain.

An inverse method based on the experimental data from ref. [7] was used to determine the weighting factor  $w$  in Eq. 20. Figure 7 shows that the CPFEM simulations agreed well with experiments over the full experimental strain range with  $w = 1$  for  $K_{iso}$ -based and  $w = 0.33$  for  $K_{aniso}$ -based calculations of  $\tau_c^{\alpha,es}$ . Note that Eq. 20 produced new resolved shear stress-strain curves, based on which new sets of  $\tau_0$  and  $h_0$  values were determined. The new parameter values are summarized in Table 4. As discussed in Section 3.2, the saturation stress ( $\tau_s$  in Eq. 5) cannot be determined from DFT-based calculations; therefore,  $\tau_s$  was calibrated to be 300 MPa based on the experimental data in Figure 7b.

The wire tension tests performed by Haasen [2] were simulated again using the newly determined parameters that consider the influence of both edge and screw dislocations with plastic deformation. Figure 8 shows that the new CPFEM predictions of Haasen's tests agreed with the experimental results up to large strains. This shows that, even though DFT-based predictions were made for pure edge and/or pure screw dislocations, the effect of both types of dislocations can be combined through Eq. 20 to capture experimental stress-strain responses of single crystals under uniaxial tension at finite deformation.

#### 4. Conclusions

In the present work, a multiscale approach has been proposed to predict the macroscopic stress-strain behavior of pure Ni single crystal. Instead of calibrating CPFEM model parameters solely using macroscopic experimental results, the present CPFEM simulations employed DFT-based

first-principles calculations of Peierls stresses at 0 K in terms of the predicted ideal shear strength and elastic properties. The conclusions of the present work are:

- The present DFT-based calculations of pure Ni shear deformation indicated that ideal shear strength of fcc Ni (also true for other materials) is layer-dependent, decreasing with increasing atomic layers due to the decreased bonding between atoms revealed by phonon calculations.
- Initial Peierls stresses without pre-strain predicted based on pure edge dislocations at 0 K matched well with experimental initial critical resolved shear stress values at room temperature, which is in line with experimental observations of the dominance of edge dislocations in stage I of fcc single crystal deformation.
- Interactions of dislocation from different slip systems can be imitated in DFT-based calculations, through the application of pre-strains, which can be used to predict Peierls stresses for edge and screw dislocations as a function of unit cell deformation. Combining DFT-based predictions for edge dislocations with CPFEM simulations, the predicted strain hardening behavior of pure Ni single crystal agreed with experiments only at small strains because the formation of jogs, which have components of screw dislocations, begin to contribute to deformation at large strains.
- At large strains, both edge and screw dislocations are present in pure Ni single crystals due to the formation of jogs. A simple model is proposed to consider the mixture of dislocations at large strains. With this combination, the present work accurately predicts the strain hardening of Ni single crystal through large deformations.

## **ACKNOWLEDGMENTS**

This work was financially supported by the U. S. Department of Energy (DOE) via award no. DE-FE0031553 and the Office of Naval Research (ONR) via contract no. N00014-17-1-2567. First-principles calculations were carried out partially on the ACI clusters at the Pennsylvania State University, partially on the resources of NERSC supported by the DOE Office of Science under contract no. DE-AC02-05CH11231, and partially on the resources of XSEDE supported by NSF via grant no. ACI-1548562.

## Figures

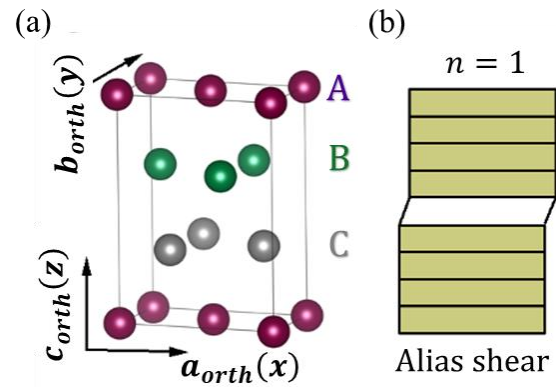


**Figure 1.** (a) Three-layer six-atom orthorhombic supercell of fcc lattice with its lattice vectors  $\mathbf{a}_{orth}(x)$ ,  $\mathbf{b}_{orth}(y)$ , and  $\mathbf{c}_{orth}(z)$  parallel to the  $[\mathbf{11\bar{2}}]$ ,  $[\bar{\mathbf{1}}\mathbf{1}\mathbf{0}]$ , and  $[\mathbf{111}]$  directions of the conventional fcc lattice; where the letters A, B, and C indicate three closed packed (111) planes. (b) Schematic diagrams of alias shear with atoms in only one plane involved in shear (i.e., the number of involved atomic planes,  $n$ , is one, shown as the unshaded area).

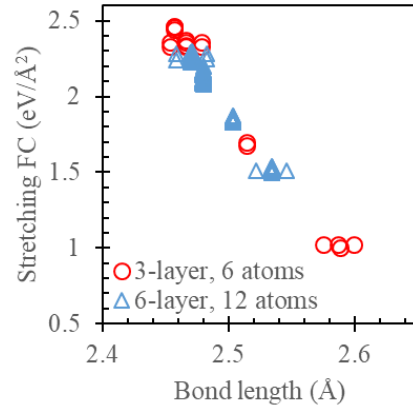


**Figure 2.** Stretching force constants (FCs) as a function of bond length for two fcc lattices of Ni: (i) the orthorhombic lattice with 3 layers and 6 atoms (see **Figure 1**), and (ii) the orthorhombic lattice with 6 layers and 12 atoms. Note that both lattices have the same shear displacement of 0.5 Å for the  $\{111\}\langle 11\bar{2}\rangle$  shear deformation, and the 72-atom supercells were employed for phonon calculations of both lattices.

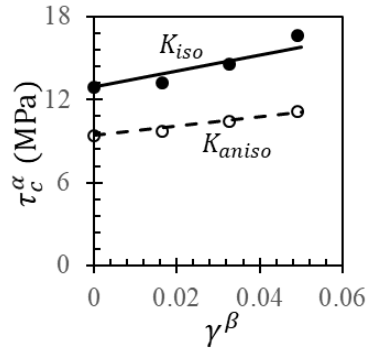


**Figure 3:** Critical resolved shear stress on slip system  $\alpha$  as a function of shear strain on slip system  $\beta$ . Symbols represent DFT-based predictions for edge dislocations, and lines show the corresponding CPFEM model curves.  $K_{iso}$  and  $K_{aniso}$  are the elastic factors used to calculate the Peierls stress (see Eq. 7).

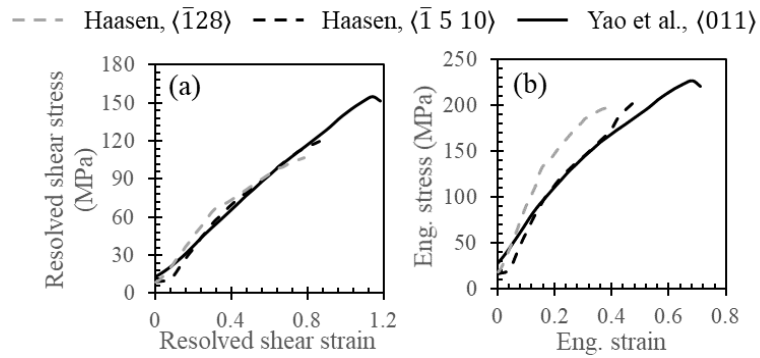
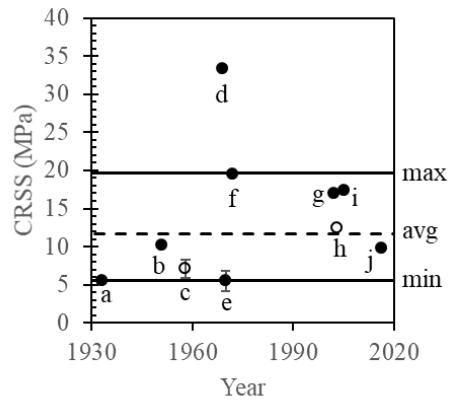


**Figure 4:** (a) Resolved shear stress vs. resolved shear strain and (b) engineering stress vs. engineering strain for pure Ni bulk single crystals in literature [2,7]. The crystallographic directions in the legend indicate the loading direction during the tests.



- a: Osswald (99.7 wt.% Ni) [69],
- b: Andrade et al. (99.9 wt.% Ni) [70],
- c: Haasen (99.999 wt.% Ni) [2],
- d: Latanision et al. (99.8 wt.% Ni) [80],
- e: Venkatesan et al. (unknown purity) [71],
- f: KondratEv et al. (99.999 wt.% Ni) [72],
- g: Hecker et al. (99.99 wt.% Ni) [73],
- h: Yao et al. (99.999 wt.% Ni) [7],
- i: Dimiduk et al., (unknown purity) [3],
- j: Luo et al. (99.99 wt.% Ni) [74].

**Figure 5:** Initial CRSS values of pure Ni reported in the literature. The value reported in ref. [80] was significantly higher than others and was excluded from the present study. The open symbols (c and h) correspond to the studies adopted in the present study for validation of CPFEM predictions.

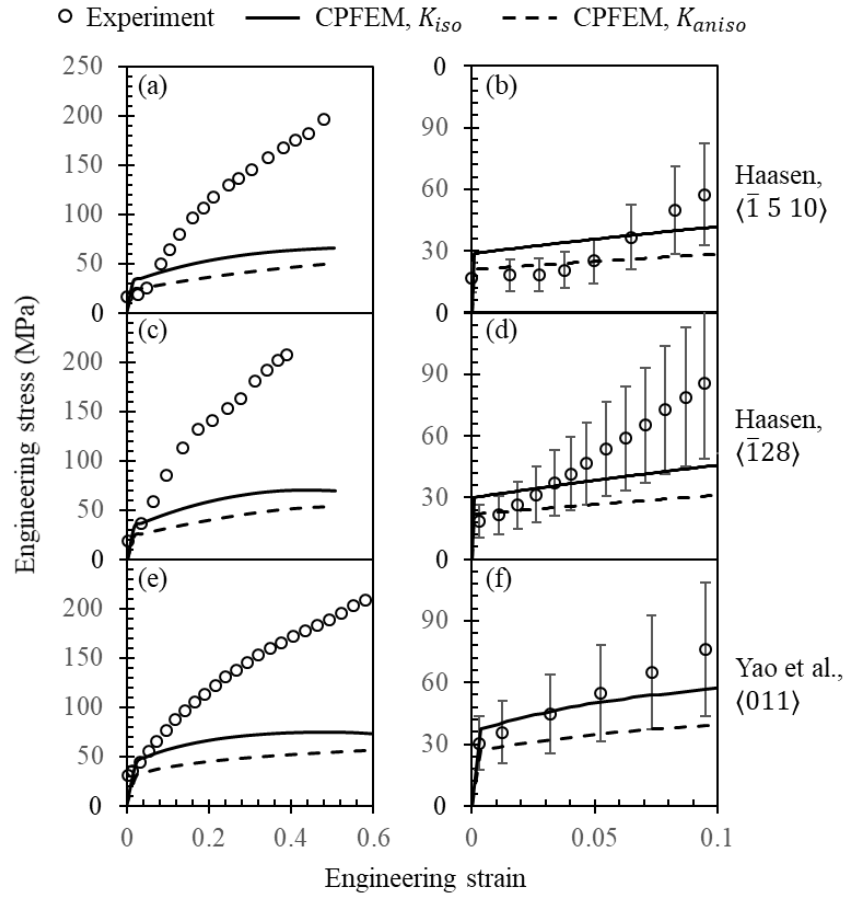


**Figure 6:** CPFEM predicted engineering stress-strain curves for (a-d) Haasen's tests [2] and (e-f) Yao et al.'s test [7] from edge dislocation based Peierls stress with an isotropic elastic factor  $K_{iso}$  (solid line) and anisotropic elastic factor  $K_{aniso}$  (dash line) compared to experimental results (symbols) by Haasen et al. [2] and Yao et al. [7].

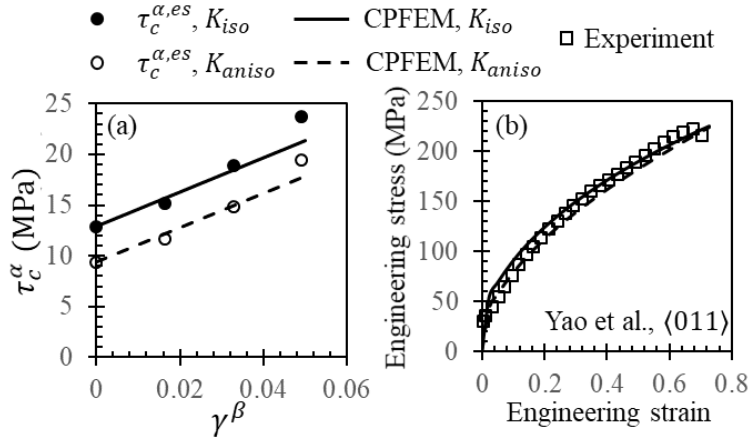


**Figure 7:** (a) Peierls stresses,  $\tau_c^{\alpha,es}$ , on slip system  $\alpha$  that combine contributions from both edge and screw dislocations as a function of shear strain on slip system  $\beta$ . The Peierls stresses (symbols) were calculated using both anisotropic and isotropic elastic factors,  $K_{aniso}$  and  $K_{iso}$ , and the corresponding CPFEM fits are also shown (lines). (b) CPFEM simulated engineering stress-strain curves (lines) of Yao et al.'s test [7] and the corresponding experimental results (symbols).

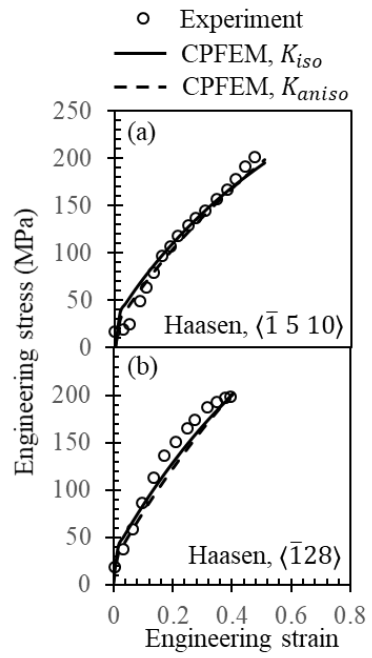


**Figure 8:** Engineering stress-strain curves for tests in ref. [2] (symbols) compared to CPFEM predictions (lines) for the combined edge and screw predictions by DFT-based calculations (see Eq. 20).

## Tables

**Table 1.** Ideal shear strength ( $\tau_{IS}$ ), associated slip (displacement) distance on the shear plane, and engineering shear strain  $\gamma_{112}$  of fcc Ni due to pure alias shear along  $\{111\}\langle 11\bar{2}\rangle$  using supercells with different layers, with the total number of atoms within each supercell given.

Supercell	Slip distance (Å)	Shear strain $\gamma_{112}$	$\tau_{IS}$ (GPa)
3-layer (6 atoms)	0.78	0.13	5.15
6-layer (12 atoms)	0.80	0.07	3.61
9-layer (18 atoms)	0.80	0.04	2.60

**Table 2.** Ideal shear strength ( $\tau_{IS}$ ) of fcc Ni due to pure alias shear of  $\{111\}\langle 11\bar{2}\rangle$  with pre-strain  $\gamma_{110}$  along the  $[\bar{1}10]$  direction, together with the predicted Peierls stresses ( $\tau_P$ , MPa) at 0 K for isotropic (iso-) and anisotropic (aniso-) edge (e) and screw (s) dislocations in comparison with experimental CRSS values ( $\tau_{CRSS}$ , MPa) at room temperature.

Properties	$\gamma_{110} = 0.000$	$\gamma_{110} = 0.016$	$\gamma_{110} = 0.033$	$\gamma_{110} = 0.049$
$\gamma_{112}$ <sup>a</sup>	0.128 (0.780)	0.126 (0.770)	0.124 (0.754)	0.120 (0.732)
$\tau_{IS}$ (in GPa)	5.15	5.16	5.19	5.26
$\tau_P$ (iso-e) <sup>b</sup>	12.9	13.2	14.6	16.6
$\tau_P$ (iso-s) <sup>b</sup>	117.7	120.3	128.4	142.4
$\tau_P$ (aniso-e) <sup>b</sup>	9.4	9.7	10.4	11.1
$\tau_P$ (aniso-s) <sup>b</sup>	308.7	318.6	362.1	457.5
$\tau_0$ (Expt.)	5.5 ~ 19.6 <sup>c</sup>			

<sup>a</sup> Engineering shear strain  $\epsilon_{112}$  corresponding to  $\tau_{IS}$ , where the slip distances (Å) on the shear plane are in the parentheses.

<sup>b</sup> By Eq. 7 with the input of  $\tau_{IS}$  in this Table,  $c_{ij}$  in Table 3, and lattice parameter  $a_0 = 3.52$  Å for fcc Ni from the present first-principles calculations.

<sup>c</sup> The range of CRSS values for Ni reported in [2,3,7,69–74]; see details in Figure 5.

**Table 3.** Calculated elastic constants (in GPa) of fcc Ni in terms of the conventional cubic lattice ( $c_{ij,\text{cub}}$ ) and the orthorhombic lattice ( $c'_{ij,\text{orth}}$ , see Figure 1a for the supercell) without and with pre-strain  $\gamma_{110}$ .

$c_{ij,\text{cub}}$ translated directly from $c'_{ij,\text{orth}}$ <sup>a</sup> $\begin{pmatrix} 265 & 161 & 161 & 0 & 0 & 0 \\ & 265 & 161 & 0 & 0 & 0 \\ & & 265 & 0 & 0 & 0 \\ & & & 127 & 0 & 0 \\ & & & & 127 & 0 \\ & & & & & 127 \end{pmatrix}$	
$c'_{ij,\text{orth}}$ without pre-strain $\gamma_{110} = 0.000$ $\begin{pmatrix} 340 & 137 & 113 & 0 & 32 & 0 \\ & 340 & 113 & 0 & -32 & 0 \\ & & 365 & 0 & 0 & 0 \\ & & & 79 & 0 & -32 \\ & & & & 79 & 0 \\ & & & & & 101 \end{pmatrix}$	$c'_{ij,\text{orth}}$ with pre-strain $\gamma_{110} = 0.016$ $\begin{pmatrix} 339 & 138 & 114 & 0 & 32 & -4 \\ & 339 & 114 & 0 & -32 & 0 \\ & & 367 & -8 & 0 & 6 \\ & & & 79 & 6 & -32 \\ & & & & 79 & 0 \\ & & & & & 102 \end{pmatrix}$
$c'_{ij,\text{orth}}$ with pre-strain $\gamma_{110} = 0.033$ $\begin{pmatrix} 338 & 137 & 113 & 0 & 31 & -9 \\ & 339 & 113 & 0 & -31 & 0 \\ & & 365 & -16 & 0 & 12 \\ & & & 78 & 12 & -31 \\ & & & & 78 & 0 \\ & & & & & 102 \end{pmatrix}$	$c'_{ij,\text{orth}}$ with pre-strain $\gamma_{110} = 0.049$ $\begin{pmatrix} 341 & 137 & 112 & -1 & 31 & -13 \\ & 341 & 112 & -1 & -31 & 1 \\ & & 365 & -23 & -2 & 17 \\ & & & 76 & 17 & -31 \\ & & & & 76 & 0 \\ & & & & & 102 \end{pmatrix}$

<sup>a</sup> Experimental elastic constants extrapolated to 0 K [56]:  $c_{11} = 261.2$ ,  $c_{12} = 150.8$ , and  $c_{44} = 131.7$  GPa.

**Table 4:** CPFEM parameter values (see Eq. 14), where  $K_{iso}$  and  $K_{aniso}$  are the elastic factors used to predict Peierls stress (see Eq. 7), and  $c_{ij}$  are elastic constants of fcc Ni reported in Table 3.

		$c_{11}$ (GPa)	$c_{12}$ (GPa)	$c_{44}$ (GPa)	$h_0$ (MPa)	$\tau_0$ (MPa)	$\tau_s$ (MPa)
Edge based	$K_{iso}$	265	161	127	41	13	40 <sup>a</sup>
	$K_{aniso}$				24	9	
Edge screw mix	$K_{iso}$				120	13	300
	$K_{aniso}$				120	9	300

<sup>a</sup> Instead of determining through the present computational approach, this value was taken from the literature [5].

**Table 5:** Statistics of the initial CRSS values in **Figure 5**. The outlier reported in ref. [80] is excluded.

Max	Min	Average	Std. Dev.	Relative error
19.6 MPa	5.5 MPa	11.66 MPa	5.01 MPa	43%

**Table 6:** Initial yield stresses (in MPa) from pure Ni single crystal tests by Haasen et al. [2] and Yao et al. [7] together with the corresponding CPFEM predictions in the present work.  $K_{iso}$  and  $K_{aniso}$  are the elastic factors used to predict Peierls stress (see Eq. 7).

Experimental value		Haasen, $\langle \bar{1} 5 10 \rangle$	Haasen, $\langle \bar{1} 28 \rangle$	Yao et al. $\langle 011 \rangle$
		17	19	31
CPFEM	$K_{iso}$	29	30	37
	$K_{aniso}$	21	22	27
Error compared to experiment	$K_{iso}$	70%	62%	22%
	$K_{aniso}$	24%	18%	12%

## References

- [1] K. S. Havner, *Finite plastic deformation of crystalline solids*. Cambridge University Press, 1992.
- [2] P. Haasen, “Plastic deformation of nickel single crystals at low temperatures,” *Philos. Mag.*, vol. 3, no. 28, pp. 384–418, 1958.
- [3] D. M. Dimiduk, M. D. Uchic, and T. A. Parthasarathy, “Size-affected single-slip behavior of pure nickel microcrystals,” *Acta Mater.*, vol. 53, no. 15, pp. 4065–4077, 2005.
- [4] C. P. Frick, B. G. Clark, S. Orso, A. S. Schneider, and E. Arzt, “Size effect on strength and strain hardening of small-scale [1 1 1] nickel compression pillars,” *Mater. Sci. Eng. A*, vol. 489, no. 1–2, pp. 319–329, 2008.
- [5] X. Zhang and F. Shang, “A continuum model for intermittent deformation of single crystal micropillars,” *Int. J. Solids Struct.*, vol. 51, no. 10, pp. 1859–1871, 2014.
- [6] C. Keller, A. M. Habraken, and L. Duchene, “Finite element investigation of size effects on the mechanical behavior of nickel single crystals,” *Mater. Sci. Engng A*, vol. 550, pp. 342–349, 2012.
- [7] Z. Yao, R. Schäublin, and M. Victoria, “Irradiation induced behavior of pure Ni single crystal irradiated with high energy protons,” *J. Nucl. Mater.*, vol. 323, no. 2–3, pp. 388–393, 2003.
- [8] F. Roters, P. Eisenlohr, L. Hantcherli, D. D. Tjahjanto, T. R. Bieler, and D. Raabe, “Overview of constitutive laws, kinematics, homogenization and multiscale methods in crystal plasticity finite-element modeling: Theory, experiments, applications,” *Acta Mater.*, vol. 58, no. 4, pp. 1152–1211, 2010.
- [9] B. Eidel, “Crystal plasticity finite-element analysis versus experimental results of pyramidal indentation into (0 0 1) fcc single crystal,” *Acta Mater.*, vol. 59, no. 4, pp. 1761–1771, 2011.
- [10] C. Zambaldi, F. Roters, D. Raabe, and U. Glatzel, “Modeling and experiments on the indentation deformation and recrystallization of a single-crystal nickel-base superalloy,” *Mater. Sci. Eng. A*, vol. 454–455, pp. 433–440, 2007.

- [11] S. Kotha, D. Ozturk, and S. Ghosh, “Parametrically homogenized constitutive models (PHCMs) from micromechanical crystal plasticity FE simulations, part I: Sensitivity analysis and parameter identification for Titanium alloys,” *Int. J. Plast.*, vol. 120, no. April, pp. 296–319, 2019.
- [12] T. O. Erinosh, D. M. Collins, A. J. Wilkinson, R. I. Todd, and F. P. E. Dunne, “Assessment of X-ray diffraction and crystal plasticity lattice strain evolutions under biaxial loading,” *Int. J. Plast.*, vol. 83, pp. 1–18, 2016.
- [13] T. O. Erinosh, A. C. F. Cocks, and F. P. E. Dunne, “Texture, hardening and non-proportionality of strain in BCC polycrystal deformation,” *Int. J. Plast.*, vol. 50, pp. 170–192, 2013.
- [14] P. A. Sabnis, S. Forest, N. K. Arakere, and V. A. Yastrebov, “Crystal plasticity analysis of cylindrical indentation on a Ni-base single crystal superalloy,” *Int. J. Plast.*, vol. 51, pp. 200–217, 2013.
- [15] C. Keller, E. Hug, A. M. Habraken, and L. Duchene, “Finite element analysis of the free surface effects on the mechanical behavior of thin nickel polycrystals,” *Int. J. Plast.*, vol. 29, no. 1, pp. 155–172, 2012.
- [16] T. Ohashi, R. I. Barabash, J. W. L. Pang, G. E. Ice, and O. M. Barabash, “X-ray microdiffraction and strain gradient crystal plasticity studies of geometrically necessary dislocations near a Ni bicrystal grain boundary,” *Int. J. Plast.*, vol. 25, no. 5, pp. 920–941, 2009.
- [17] M. G. Lee, H. Lim, B. L. Adams, J. P. Hirth, and R. H. Wagoner, “A dislocation density-based single crystal constitutive equation,” *Int. J. Plast.*, vol. 26, no. 7, pp. 925–938, 2010.
- [18] A. Shahba and S. Ghosh, “Crystal plasticity FE modeling of Ti alloys for a range of strain-rates. Part I: A unified constitutive model and flow rule,” *Int. J. Plast.*, vol. 87, pp. 48–68, 2016.
- [19] S. Ghosh, A. Shahba, X. Tu, E. L. Huskins, and B. E. Schuster, “Crystal plasticity FE modeling of Ti alloys for a range of strain-rates. Part II: Image-based model with experimental validation,” *Int. J. Plast.*, vol. 87, pp. 69–85, 2016.

- [20] A. Ma and F. Roters, “A constitutive model for fcc single crystals based on dislocation densities and its application to uniaxial compression of aluminium single crystals,” *Acta Mater.*, vol. 52, no. 12, pp. 3603–3612, 2004.
- [21] E. Renner, Y. Gaillard, F. Richard, F. Amiot, and P. Delobelle, “Sensitivity of the residual topography to single crystal plasticity parameters in Berkovich nanoindentation on FCC nickel,” *Int. J. Plast.*, vol. 77, pp. 118–140, 2016.
- [22] D. Ma, M. Friák, J. Neugebauer, D. Raabe, and F. Roters, “Multiscale simulation of polycrystal mechanics of textured  $\beta$ -Ti alloys using ab initio and crystal-based finite element methods,” *Phys. Status Solidi*, vol. 245, no. 12, pp. 2642–2648, 2008.
- [23] C. R. Weinberger, C. C. Battaile, T. E. Buchheit, and E. A. Holm, “Incorporating atomistic data of lattice friction into BCC crystal plasticity models,” *Int. J. Plast.*, vol. 37, pp. 16–30, 2012.
- [24] U. F. Kocks and H. Mecking, “Physics and phenomenology of strain hardening : the FCC case,” *Prog. Mater. Sci.*, vol. 48, pp. 171–273, 2003.
- [25] B. Devincere, T. Hoc, and L. Kubin, “Dislocation Mean Free Paths and Strain Hardening of Crystals,” *Science (80-. )*, vol. 320, no. 5884, pp. 1745–1748, 2008.
- [26] J. S. Langer, E. Bouchbinder, and T. Lookman, “Thermodynamic theory of dislocation-mediated plasticity,” *Acta Mater.*, vol. 58, no. 10, pp. 3718–3732, 2010.
- [27] V. Bulatov, F. F. Abraham, L. Kubin, B. Devincere, and S. Yip, “Connecting atomistic and mesoscale simulations of crystal plasticity,” *Nature*, vol. 391, no. 6668, pp. 669–672, 1998.
- [28] A. Vattré, B. Devincere, F. Feyel, R. Gatti, S. Groh, O. Jamond, and A. Roos, “Modelling crystal plasticity by 3D dislocation dynamics and the finite element method: The Discrete-Continuous Model revisited,” *J. Mech. Phys. Solids*, vol. 63, no. 1, pp. 491–505, 2014.
- [29] Z. L. Liu, Z. Zhuang, X. M. Liu, X. C. Zhao, and Z. H. Zhang, “A dislocation dynamics based higher-order crystal plasticity model and applications on confined thin-film plasticity,” *Int. J. Plast.*, vol. 27, no. 2, pp. 201–216, 2011.
- [30] T. Hochrainer, S. Sandfeld, M. Zaiser, and P. Gumbsch, “Continuum dislocation dynamics:

- Towards a physical theory of crystal plasticity,” *J. Mech. Phys. Solids*, vol. 63, no. 1, pp. 167–178, 2014.
- [31] F. R. N. Nabarro, “Fifty-year study of the Peierls-Nabarro stress,” *Mater. Sci. Eng. A*, vol. 234–236, pp. 67–76, Aug. 1997.
- [32] J. N. Wang, “Prediction of Peierls stresses for different crystals,” *Mater. Sci. Eng. A*, vol. 206, no. 2, pp. 259–269, 1996.
- [33] J. W. Steeds, “Dislocation arrangement in copper single crystals as a function of strain,” *Proc. R. Soc. London. Ser. A. Math. Phys. Sci.*, vol. 292, no. 1430, pp. 343–373, 1966.
- [34] Z. S. Basinski, “Dislocation distribution in deformed copper single crystals,” *Philos. Mag.*, vol. 9, no. 97, pp. 51–80, 1964.
- [35] H. P. Karnthaler, E. T. Mühlbacher, and C. Rentenberger, “The influence of the fault energies on the anomalous mechanical behaviour of Ni3Al alloys,” *Acta Mater.*, vol. 44, no. 2, pp. 547–560, Feb. 1996.
- [36] M. Zehetbauer and V. Seumer, “Cold work hardening in stages IV and V of FCC metals—I. Experiments and interpretation,” *Acta Metall. Mater.*, vol. 41, no. 2, pp. 577–588, 1993.
- [37] J. W. Steeds and P. M. Hazzledine, “Dislocation configurations in deformed copper and copper 10% (atomic) aluminium alloy,” *Discuss. Faraday Soc.*, vol. 38, pp. 103–110, 1964.
- [38] E. de Souza Neto, D. Peric, and D. R. J. Owen, *Computational Methods for Plasticity*, vol. 55. 2008.
- [39] S. R. Kalidindi and L. Anand, “Macroscopic shape change and evolution of crystallographic texture in pre-textured FCC metals,” *J. Mech. Phys. Solids*, vol. 42, no. 3, pp. 459–490, 1994.
- [40] A. F. Bower, *Applied mechanics of solids*. CRC press, 2009.
- [41] Y. Huang, “A User-Material Subroutine Incorporating Single Crystal Plasticity in the ABAQUS Finite Element Program,” *Harvard Univ.*, no. Jun, 1991.
- [42] G. P. Potirniche, J. L. Hearndon, M. F. Horstemeyer, and X. W. Ling, “Lattice orientation

- effects on void growth and coalescence in fcc single crystals,” *Int. J. Plast.*, vol. 22, no. 5, pp. 921–942, 2006.
- [43] S. R. Kalidindi and S. E. Schoenfeld, “On the prediction of yield surfaces by the crystal plasticity models for fcc polycrystals,” *Mater. Sci. Eng. A*, vol. 293, no. 1, pp. 120–129, 2000.
- [44] D. Peirce, R. J. J. Asaro, and A. Needleman, “An analysis of nonuniform and localized deformation in ductile single crystals,” *Acta Metall.*, vol. 30, no. 6, pp. 1087–1119, Jun. 1982.
- [45] S. Ogata, J. Li, and S. Yip, “Ideal pure shear strength of aluminum and copper,” *Science (80-. )*, vol. 298, no. 5594, pp. 807–811, 2002.
- [46] T. H. Wille and C. Schwink, “Precision measurements of critical resolved shear stress in CuMn alloys,” *Acta Metall.*, vol. 34, no. 6, pp. 1059–1069, 1986.
- [47] S.-L. Shang, Y. Wang, T. J. Anderson, and Z.-K. Liu, “Achieving accurate energetics beyond (semi-) local density functional theory: Illustrated with transition metal disulfides, Cu<sub>2</sub>ZnSnS<sub>4</sub>, and Na<sub>3</sub>PS<sub>4</sub> related semiconductors,” *Phys. Rev. Mater.*, vol. 3, no. 1, p. 015401, Jan. 2019.
- [48] S.-L. Shang, Y. Wang, D. Kim, and Z.-K. Liu, “First-principles thermodynamics from phonon and Debye model: Application to Ni and Ni<sub>3</sub>Al,” *Comput. Mater. Sci.*, vol. 47, no. 4, pp. 1040–1048, Feb. 2010.
- [49] S. L. Shang, W. Y. Wang, Y. Wang, Y. Du, J. X. Zhang, A. D. Patel, and Z. K. Liu, “Temperature-dependent ideal strength and stacking fault energy of fcc Ni: a first-principles study of shear deformation,” *J. Phys. Condens. Matter*, vol. 24, no. 15, p. 155402, Apr. 2012.
- [50] B. Joós and M. S. Duesbery, “The Peierls Stress of Dislocations: An Analytic Formula,” *Phys. Rev. Lett.*, vol. 78, no. 2, pp. 266–269, Jan. 1997.
- [51] J. P. Hirth and J. Lothe, *Theory of dislocations*. Krieger Pub. Co, 1992.
- [52] S. L. Shang, W. Y. Wang, B. C. Zhou, Y. Wang, K. A. Darling, L. J. Kecskes, S. N.

- Mathaudhu, and Z. K. Liu, “Generalized stacking fault energy, ideal strength and twinnability of dilute Mg-based alloys: A first-principles study of shear deformation,” *Acta Mater.*, vol. 67, pp. 168–180, 2014.
- [53] M. Jahnatek, J. Hafner, M. Krajci, M. Jahnátek, J. Hafner, and M. Krajčí, “Shear deformation, ideal strength, and stacking fault formation of fcc metals: A density-functional study of Al and Cu,” *Phys. Rev. B*, vol. 79, no. 22, p. 224103, Jun. 2009.
- [54] S. L. Shang, Y. Wang, and Z. K. Liu, “First-principles elastic constants of alpha- and theta-Al<sub>2</sub>O<sub>3</sub>,” *Appl. Phys. Lett.*, vol. 90, no. 10, p. 101909, 2007.
- [55] S. L. Shang, D. E. Kim, C. L. Zacherl, Y. Wang, Y. Du, and Z. K. Liu, “Effects of alloying elements and temperature on the elastic properties of dilute Ni-base superalloys from first-principles calculations,” *J. Appl. Phys.*, vol. 112, no. 5, p. 053515, Sep. 2012.
- [56] G. Simmons and H. Wang, *Single crystal elastic constants and calculated aggregate properties: A handbook*. Cambridge: M.I.T. Press, 1971.
- [57] G. Kresse and J. Furthmüller, “Efficient iterative schemes for ab initio total-energy calculations using a plane-wave basis set,” *Phys. Rev. B*, vol. 54, no. 16, pp. 11169–11186, 1996.
- [58] G. Kresse and D. Joubert, “From ultrasoft pseudopotentials to the projector augmented-wave method,” *Phys. Rev. B*, vol. 59, no. 3, pp. 1758–1775, 1999.
- [59] J. P. Perdew, J. A. Chevary, S. H. Vosko, K. A. Jackson, M. R. Pederson, D. J. Singh, and C. Fiolhais, “Atoms, molecules, solids, and surfaces: Applications of the generalized gradient approximation for exchange and correlation,” *Phys. Rev. B*, vol. 46, no. 11, pp. 6671–6687, Sep. 1992.
- [60] M. Methfessel and A. T. Paxton, “High-precision sampling for Brillouin-zone integration in metals,” *Phys. Rev. B*, vol. 40, no. 6, pp. 3616–3621, Aug. 1989.
- [61] T. Bučko, J. Hafner, and J. G. Ángyán, “Geometry optimization of periodic systems using internal coordinates,” *J. Chem. Phys.*, vol. 122, no. 12, p. 124508, Mar. 2005.
- [62] Y. Wang, J. J. Wang, W. Y. Wang, Z. G. Mei, S. L. Shang, L. Q. Chen, and Z. K. Liu, “A

- mixed-space approach to first-principles calculations of phonon frequencies for polar materials,” *J. Phys. Condens. Matter*, vol. 22, no. 20, p. 202201, May 2010.
- [63] Y. Wang, S.-L. Shang, H. Fang, Z.-K. Liu, and L.-Q. Chen, “First-principles calculations of lattice dynamics and thermal properties of polar solids,” *npj Comput. Mater.*, vol. 2, no. 1, p. 16006, Nov. 2016.
- [64] Y. Wang, L.-Q. Chen, and Z.-K. Liu, “YPHON: A package for calculating phonons of polar materials,” *Comput. Phys. Commun.*, vol. 185, no. 11, pp. 2950–2968, Nov. 2014.
- [65] D. Lorenz, A. Zeckzer, U. Hilpert, P. Grau, H. Johansen, and H. S. Leipner, “Pop-in effect as homogeneous nucleation of dislocations during nanoindentation,” *Phys. Rev. B*, vol. 67, no. 17, p. 172101, May 2003.
- [66] C. R. Krenn, D. Roundy, M. L. Cohen, D. C. Chrzan, and J. W. Morris, “Connecting atomistic and experimental estimates of ideal strength,” *Phys. Rev. B*, vol. 65, no. 13, p. 134111, Mar. 2002.
- [67] S.-L. Shang, Y. Wang, B. Gleeson, and Z.-K. Liu, “Understanding slow-growing alumina scale mediated by reactive elements: Perspective via local metal-oxygen bonding strength,” *Scr. Mater.*, vol. 150, pp. 139–142, Jun. 2018.
- [68] S. L. Shang, L. G. Hector Jr, Y. Wang, H. Zhang, and Z. K. Liu, “First-principles study of elastic and phonon properties of the heavy fermion compound CeMg,” *J. Phys. Condens. Matter*, vol. 21, no. 24, p. 246001, Jun. 2009.
- [69] V. E. Osswald, “Zugversuche an Kupfer-Nickelkristallen,” *Zeitschrift für Phys. A Hadron. Nucl.*, vol. 1, no. 83, pp. 55–78, 1933.
- [70] E. N. da C. Andrade and C. Henderson, “The Mechanical Behaviour of Single Crystals of Certain Face-Centered Cubic Metals,” *Philos. Trans. R. Soc. London A*, vol. 244, no. 880, pp. 177–203, 1951.
- [71] P. S. Venkatesan and D. N. Beshers, “Plastic deformation in nickel crystals,” *Metall. Trans.*, vol. 1, no. 6, pp. 1780–1782, 1970.
- [72] E. F. Kondrat’ev and A. V. Pets, “Ferromagnetic resonance in plastically deformed nickel

- monocrystals,” *Sov. Phys. J.*, vol. 15, no. 2, pp. 242–244, 1972.
- [73] M. Hecker, E. Thiele, and C. Holste, “Investigation of the tensor character of mesoscopic internal stresses in tensile-deformed nickel single crystals by X-ray diffraction,” *Acta Mater.*, vol. 50, no. 9, pp. 2357–2365, 2002.
- [74] Y. Luo, J. Liu, W. Guo, Q. Yu, and S. Li, “Dislocation Slip Behavior of Ni Single Crystal Under Dynamic Compression,” *J. Dyn. Behav. Mater.*, vol. 2, no. 2, pp. 223–233, 2016.
- [75] J. F. Bell, *The Physics of Large Deformation of Crystalline Solids*. Springer, 1968.
- [76] D. K. Bowen and J. W. Christian, “The calculation of shear stress and shear strain for double glide in tension and compression,” *Philos. Mag.*, vol. 12, no. 116, pp. 369–378, 1965.
- [77] R. Honeycombe, *The plastic deformation of metals*. 1968.
- [78] Z. Yao, “The relationship between the irradiation induced damage and the mechanical properties of single crystal Ni,” EPFL, 2005.
- [79] F. v. Göler and G. skar Sachs, “Das Verhalten von Aluminiumkristallen bei Zugversuchen,” *Zeitschrift für Phys.*, vol. 41, no. 2–3, pp. 103–115, 1927.
- [80] R. M. Latanision and R. W. Staehle, “Plastic deformation of electrochemically polarized nickel single crystals,” *Acta Metall.*, vol. 17, no. 3, pp. 307–319, 1969.
- [81] “Abaqus User Manual v2017,” *DS SIMULIA*, 2017.
- [82] J. W. Kysar, “Addendum to ‘A User-Material Subroutine Incorporating Single Crystal Plasticity in the ABAQUS Finite Element Program’, Huang, Y., Mech Report 178, Harvard University, 1991.,” *Harvard Univ. MECH Rep.*, pp. 1–3, 1997.